ADVANCED ENERGY & SUSTAINABILITY RESEARCH
Open Access
www.advenergysustres.com

Structure Properties Correlations on Nickel-Iron Oxide Catalysts Deposited by Atomic Layer Deposition for the Oxygen Evolution Reaction in Alkaline Media

*Estelle Jozwiak, Anna Phan, Thorsten Schultz, Norbert Koch, and Nicola Pinna**

Thermal atomic layer deposition (ALD) is used for the first time to deposit iron-nickel oxides onto carbon nanotubes in a ternary process to produce a wide range of mixed oxide thin films. When using ferrocene ($FeCp_2$) and nickelocene ($NiCp_2$) with ozone (O_3) as metals and oxygen sources, respectively, a competition between the metal precursors and the growth modes is observed. Indeed, while ferrocene promotes a 2D-growth, nickelocene prefers a 3D-growth. Although both precursors are homoleptic metallocenes, they behave differently in the ALD of their respective metal oxide, leading to unexpected atomic ratios and films morphologies of the iron-nickel oxides. The 2Fe:1Ni sample displays the best performances in the electrochemical water oxidation (oxygen evolution reaction) exhibiting an overpotential of 267 mV at a current density of 10 mA cm^{-1}, a Tafel slope of 36.8 mV dec^{-1}, as well as a good stability after 15 h of continuous operation.

1. Introduction

There is an increasing need for green energy alternatives to replace environmentally harmful fossil fuels. Hydrogen combusts with oxygen to generate exclusively energy and water, making it an attractive alternative to fossil fuels. However, nowadays, the primary method of H_2 production is based on steam-methane reforming.[1] Electrochemical water (EC-H_2O) splitting (overall process described in Equation (1)) is a promising process to circumvent the steam-methane reforming

$$H_2O_{(l)} \rightarrow H_{2(g)} + \frac{1}{2} O_{2(g)} \quad (1)$$

EC-H_2O splitting can be divided into two half reactions: The oxygen evolution reaction (OER) and the hydrogen evolution reaction (HER), occurring at the anode and the cathode, respectively. Among the two reactions, the OER remains challenging because it involves the transfer of 4 electrons (Equation (2))

$$4OH^-_{(aq)} \rightarrow O_{2(g)} + 2H_2O_{(l)} + 4e^- \quad (2)$$

($E°_{ox} = -1{,}23$ V, vs. RHE at 25 °C and 1 atm)

This makes the OER reaction sluggish and affects, by extension, the overall EC-H_2O splitting process.[2–4] Extensive research has established RuO_2 and IrO_2 as excellent OER catalysis anode materials in acidic media. However, the scarcity, the high price of noble metals, and their low stability have long restricted their adoption by the industry.[5–7] The need for cheaper alternatives has driven innovation and led to several promising transition metal alternatives based on earth-abundant elements such as Mn, Fe, and Ni.[8–13]

Nickel and iron-nickel oxides and specially oxyhydroxides are known as the most efficient and stable OER catalysts in alkaline media.[10–15] However, their role in the reaction is not yet fully understood. A complementary role of iron and nickel has been postulated, with nickel acting as the active site and iron being responsible for the nickel activation via partial charge transfer, while others attribute the main activity to iron edge atoms.[16–21] Thus, the precise role of each element during the OER reaction remains elusive. This lack of understanding is, however, not an obstacle to the exploration of different synthesis routes that may improve the activity of nickel-iron oxides catalysts. Indeed, to provide a good catalyst, a large surface area and a high number of active sites are required, among other parameters such as conductivity and stability. The deposition of iron-nickel oxides has already been reported few times for other applications involving highly concentrated nickel films (Ni > 83% atomic mass).[22,23] However, to obtain the best OER efficiency, an optimal relative

E. Jozwiak, N. Pinna
Department of Chemistry and the Center for the Science of Materials Berlin
Humboldt-Universität zu Berlin
12489 Berlin, Germany
E-mail: nicola.pinna@hu-berlin.de

A. Phan
UFR de Chimie
Sorbonne Université
UPMC 06, 75005 Paris, France

T. Schultz, N. Koch
Institut für Physik and IRIS Adlershof
Humboldt-Universität zu Berlin
12489 Berlin, Germany

T. Schultz, N. Koch
Helmholtz-Zentrum Berlin für Materialien und Energie GmbH
14109 Berlin, Germany

The ORCID identification number(s) for the author(s) of this article can be found under https://doi.org/10.1002/aesr.202400091.

DOI: 10.1002/aesr.202400091

percentage of iron should be reached. The optimum iron content was found to vary between 5% and 40%.[16–21] A recent article reported the deposition of nickel-iron phosphates using plasma-enhanced PE-ALD. Some similarities, such as the unexpected atomic ratio in the films, were reported supporting the findings in the present work.[9] However, the growth mode competition, film morphology, and crystallinity of the deposited films have never been investigated before. Herein, the study of iron-nickel oxide OER catalysts deposited onto carbon nanotubes (CNTs) by thermal ALD is reported.

ALD is the technique of choice to produce ultrathin films with a high reproducibility, thickness reliability, conformality, and surface coverage. ALD is based on self-limiting surface reactions making it suitable to coat conformally high aspect ratio substrates.[24–26] However, when organometallic compounds are used as precursors, a full monolayer cannot be deposited in one cycle due to the steric hindrance of the remaining ligands.[27,28] Depending on the metal and precursor used, two growth modes can occur: a 2D basal or a 3D island-like growth. These two modes lead to the formation of a smooth or a rough layer, respectively.[29–32] Thus, 2D growth modes are advantageous for depositing conformal films, while the 3D island-like growth may enhance nanoparticle growth. During 3D growth, nanoparticles may coalesce with one another, leading to a rough film or in some cases vertical growth morphologies.[33,34]

Herein, mixed nickel and iron oxides deposited from nickelocene, known to lead to a 3D-island growth,[35,36] and ferrocene, known to lead to a conformal 2D growth,[37,38] were used together with ozone as oxygen source to coat high aspect ratio hollow CNTs. A competition between the growth modes is obtained during the ALD process, leading to nonlinear atomic concentrations and growth per cycles (GPC) in the mixed oxides. The morphology of the obtained films was also affected. A decrease of the size of the nanoparticles produced during the ALD process was observed with increasing the pulse ratio of ferrocene. It will also be shown that the electrocatalytical properties depend on the composition, thin film morphologies, and crystallinity. Therefore, clear structure–properties correlations will be presented.

2. Results

2.1. Catalyst Characterization

The ALD processes showed a linear growth for both pure and mixed iron-nickel oxides on silicon wafers. On silicon wafers, pure nickel and iron oxide exhibited a growth per cycle (GPC) of 0.040 and 0.026 nm, respectively. Changes in GPC as a function of the metallic pulse ratio (**Figure 1**a) exhibit a continuous decrease until a minimum of 0.022 nm (2Fe:1Ni) is reached and then an increase with increasing Fe pulses. This trend is conserved for the deposition onto the CNT substrates (Figure 1a). Furthermore, in both cases, the GPC displays asymmetry with respect to the metal precursor pulse ratios. This suggests that there may be an unequal concentration of Ni and Fe with respect to their nominal pulse ratios. This is somewhat expected when considering the higher GPC of nickelocene to that of ferrocene (Figure 1a, 0Fe:1Ni vs 1Fe:0Ni) ALD processes. Additionally, although the GPC trend observed on silicon wafer and on the CNTs is similar, the GPC found on Si wafer is higher than the one found on CNTs. This discrepancy may be attributed to the concentration, strength, and nature of the anchoring site on the substrate surface. SiO_2 wafers are exclusively composed of hydroxyl groups on their surface, whereas CNTs contain other functional groups such as carboxylic acid and hydroxyl groups.[39] The morphological difference between the two substrates may also influence the GPC.

The relative Ni and Fe concentration was characterized by energy-dispersive X-Ray analysis (EDX) and X-Ray photoelectron spectroscopy (XPS) (**Table 1**). The results indicate that the asymmetric GPC is indeed related to a nonlinear concentration of the metals. Nickelocene pulses consistently deposit greater quantities of nickel compared to that of iron by ferrocene.

By plotting the precursor atomic ratio as a function of the atomic ratios found in EDX and XPS analysis (Figure 1c), a clear deviation from a linear fit is observed. An S-shaped curve indicates an unbalanced incorporation of nickel relative to iron. This is most evident within the plateau region, with nickel remaining the dominant element despite a larger excess of ferrocene pulses (2Fe:1Ni). At a 3:1 ratio, iron becomes the predominant element within the film. This finding may be attributed to the difference in the valence electrons between the two metallocene precursors. Ferrocene possesses a saturated valence electron shell, substituting an iron atom for a nickel atom increases the valence electron count from 18 to 20. Thus, nickelocene is destabilized relative to ferrocene, increasing the likelihood of cyclopentadienyl "ring slip" or interconversion from η^5 to a η^3 binding mode at equilibrium.[40–42] Thus, the interconversion stabilizes the metal against thermal decomposition, but increases its reactivity via the available unpaired electrons affording greater reactivity of nickelocene during ALD and could explain the nonlinearity between the number of metal pulses applied and the relative concentration of the transition metals in the films (Figure 1c).

As already reported, the use of nickelocene as a precursor leads to a 3D-island growth,[35,36] while a 2D growth is favored when using ferrocene as a precursor.[37,38] Those two different growth modes result in rough and smooth layers for nickel and iron oxide, respectively, as shown in the transmission electron microscopy (TEM) micrographs (**Figure 2**, S1, Supporting Information). Concerning the iron-nickel oxides, a 3D-island growth is preferred until the 2Fe:1Ni sample. Afterward, a 2D growth takes over the 3D-island growth leading to a smooth layer (3Fe:1Ni). The relative concentration of nickel and iron inside the films (Figure 1b) suggests that when the nickel relative atomic concentration dominates, a 3D-island growth mode is adopted. However, a transition to the 2D growth mode is preferred when the relative atomic concentration of iron is larger than 50%.

The nanoparticles formed at the surface of the CNTs in the 3D-growth regime are smaller and smoother when the iron content increases until reaching a critical value of 46:54 (EDX) of relative atomic concentration of iron and nickel, respectively (2Fe:1Ni). This trend can be explained by taking a closer look at the selected area electron diffraction (SAED) patterns shown in the Figure S4, S5 and S6, Supporting Information. All the samples displayed Debye–Scherrer concentric rings, confirming the presence of nanoparticles and indicating the polycrystalline

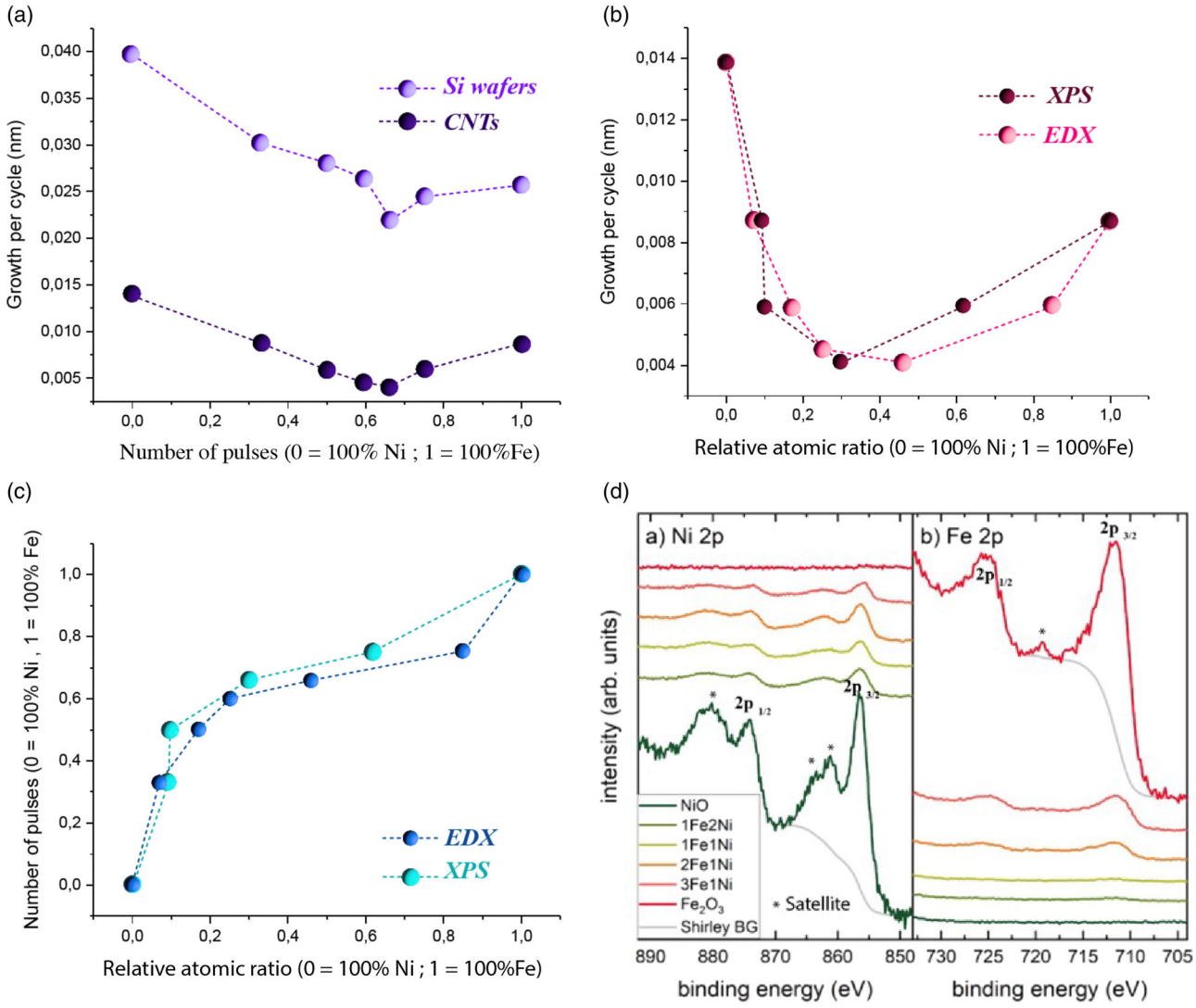

Figure 1. GPC measured a) according to the Ni/Fe metallic ratio expected, b) on CNTs according to the relative atomic ratio found for the samples with 400 metal pulses, c) atomic ratio expected as a function of the Ni/Fe relative ratio found in EDX and XPS measurements for 400 metal pulses, d) XPS measurements of the different catalysts synthesized by ALD.

Table 1. Atomic % of nickel and iron in the films by EDX and XPS for the 400 metal pulses.

Pulses ratio	Atomic % found in EDX	Atomic % found in XPS
100%Ni–0%Fe	100%Ni–0%Fe	100%Ni–0%Fe
66%Ni–33%Fe	93%Ni–7%Fe	90%Ni–10%Fe
50%Ni–50%Fe	83%Ni–17%Fe	89%Ni–11%Fe
60%Ni–40%Fe	75%Ni–25%Fe	–
33%Ni–66%Fe	54%Ni–46%Fe	70%Ni–30%Fe
25%Ni–75%Fe	15%Ni–85%Fe	40%Ni–60%Fe
0%Ni–100%Fe	0%Ni–100%Fe	0%Ni–100%Fe

nature of the deposited layers. Furthermore, NiO is recognized for crystallizing in the rock salt structure, while iron oxide deposited from ferrocene and ozone has been reported to crystallize in a corundum structure (α-Fe_2O_3), accompanied by an indeterminate structure composed of both Fe(II) and Fe(III).[43] The pure nickel and iron oxide Debye–Scherrer rings correspond to the (111), (200), (220), and (311) planes of the cubic rock salt structure of NiO and FeO (wüstite) (Figure S4, Supporting Information). The SAED patterns of the mixed iron–nickel samples were juxtaposed with those of the pure phases (Figure S4 and S5, supporting information), to help with the determination of their crystalline structure. 1Fe:2Ni and 1Fe:1Ni exhibited the same diffraction rings as NiO, suggesting that their lattice parameters are closer to those of NiO. Following the 1Fe:1Ni composition, an increase of the rings size is recorded, and the wüstite structure was observed. Indeed, a 25% iron concentration in the samples is enough to decrease the lattice parameters. An additional concentric ring was consistently observed in all samples, indicating the presence of graphitized carbon in the CNTs with its (002) hexagonal plane.

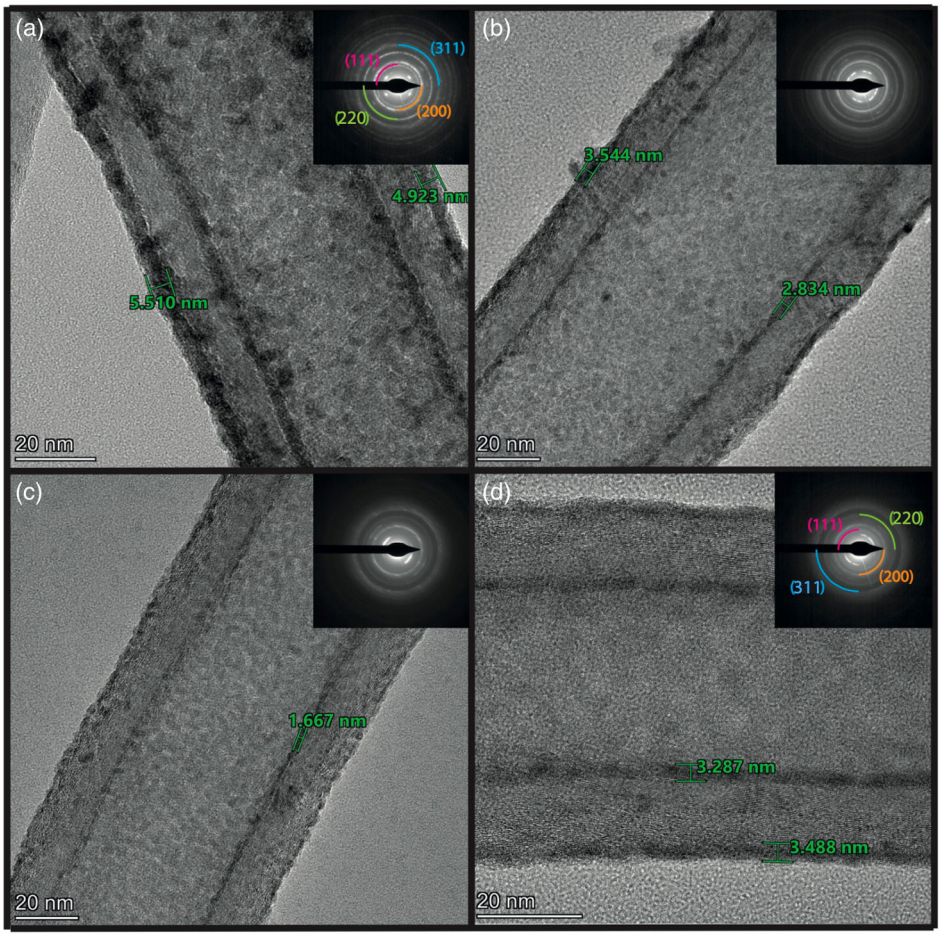

Figure 2. TEM micrographs and SAED patterns after 400 metal pulses of: a) 0Fe:1Ni; b) 1Fe:2Ni; c) 2Fe:1Ni; d) 1Fe:0Ni.

XPS was employed to analyze the surface composition of all the samples. Figure 1d, and Figure S2 and S3, Supporting Information show the Ni 2*p* and the Fe 2*p* core-level spectra, respectively. In the Ni 2*p* spectrum (Figure 1d and S2, Supporting Information), a peak corresponding to Ni $2p_{1/2}$ peak is observed at high binding energy (BE). At low BE, the Ni $2p_{3/2}$ exhibited a peak with a binding energy of ≈855.6 eV, which together with the satellite structure indicates the formation of $Ni(OH)_2$ exclusively in all the samples.[44] As previously documented, when thin NiO films formed by ALD are exposed to air, the water present will absorb dissociatively on NiO leading to hydroxyl surface species.[14] The phenomenon elucidates the observation of surface $Ni(OH)_2$ in the XPS measurement. The three other peaks are from the Ni 2*p* satellites (stars). The Figure S3, Supporting Information, exhibited 3 peaks. One at high BE corresponding to the Fe $2p_{1/2}$, one at low BE corresponding to the Fe $2p_{3/2}$, and in between the peak corresponding to Fe $2p_{3/2}$ satellite. The Fe $2p_{3/2}$ peak showed a binding energy at 710.8 eV indicating the deposition of Fe_2O_3. However, the SAED patterns (Figure S4, Supporting Information) results indicated the presence of Fe^{2+}, highlighted by the Debye–Scherrer rings of FeO in its wüstite form. A more precise XPS investigation was carried out on a fresh and thicker pure iron oxide sample to assure that the presence of Fe_2O_3 in the XPS measurements was not the consequence of a surface oxidation due to air storage (Figure S3, Supporting Information). The sample was stored and tested under a controlled atmosphere. However, an exact quantification of the iron chemical state remains challenging due to shake-up, plasmon loss structures, and mutiplet splitting.[45] The residual fitting (Figure S5, Supporting Information) showed a more accurate value when FeO was included in the analysis. The Fe $2p_{3/2}$ peak can be deconvoluted in ten different peaks (Figure S4, Supporting Information): 5 corresponding to Fe^{3+} ($2p_{3/2}$) and 5 others corresponding to Fe^{2+} ($2p_{3/2}$). After calculation, a distribution of ≈20% of Fe(+II) and ≈80% of Fe(+III) was demonstrated, suggesting the presence of 2 distinct and coexisting phases in the pure iron deposited films: a crystalline FeO and an amorphous Fe_2O_3 phase. Concerning the mixed samples, the presence of $Ni(OH)_2$, $Fe^{2+}(2p_{3/2})$, and $Fe^{3+}(2p_{3/2})$ was also found (Figure 1d and S2, Supporting Information). An increase in the intensity of the iron peaks with the increase in iron:nickel pulses ratio was also observed (and vice versa for the nickel peaks).

In addition, the elemental mappings of the iron-nickel oxides samples showed a homogeneous distribution of nickel and iron in the coated films (Figure S9, Supporting Information).

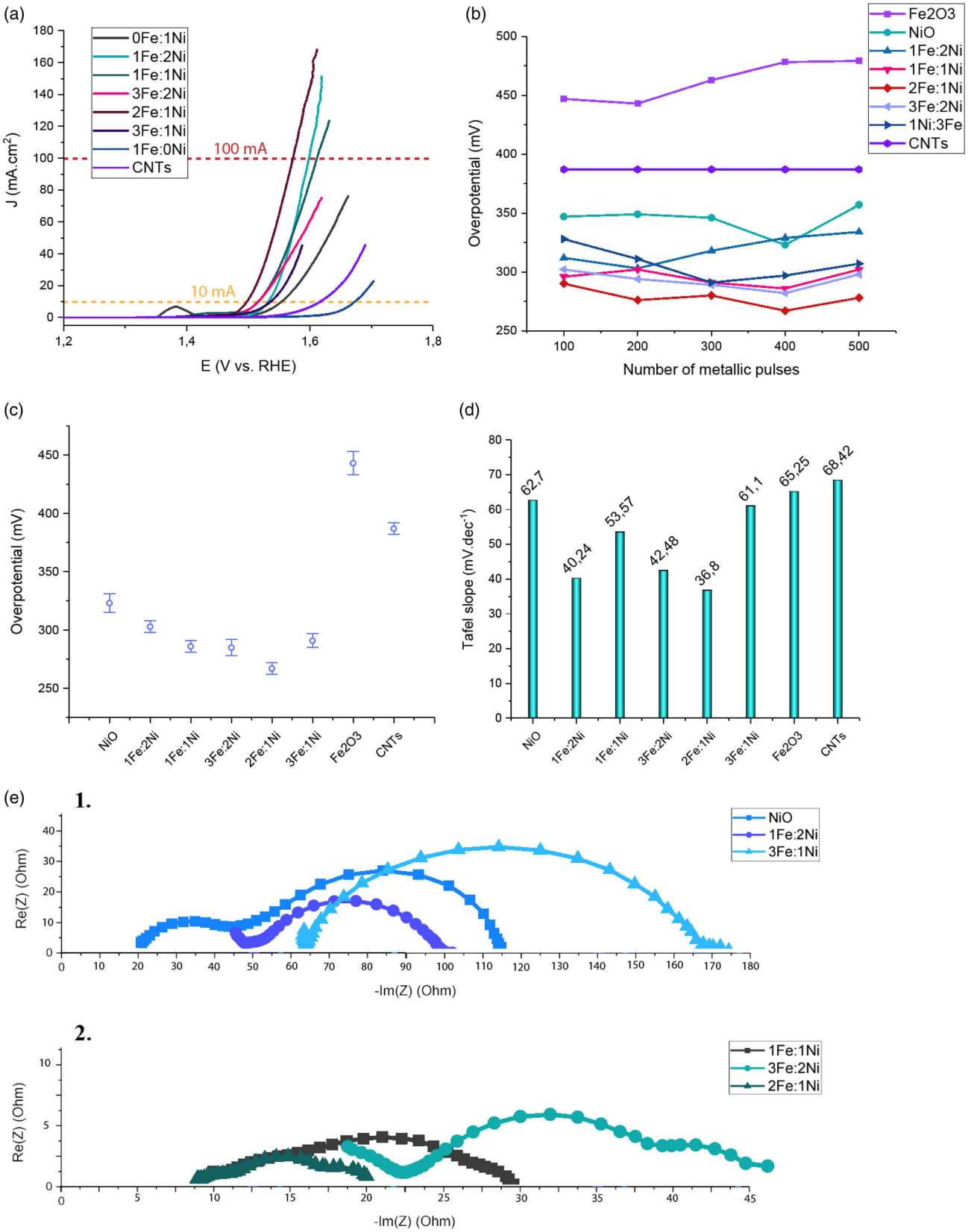

Figure 3. a) LSV curves; b) summary of all the overpotential exhibited; c) overpotentials at 10 mA cm^{-2}; d) Tafel slopes; e) 1,2 PEIS measurements exhibited by the optimized layer thicknesses.

2.2. Electrochemical Characterization

All samples underwent electrochemistry testing to determine the optimized thickness and composition to ensure the best OER catalytic activity. Indeed, a too thin layer would lead to an insufficient number of active sites at the catalyst surface, while a too thick layer would increase the resistivity of the electrode. Cyclic voltammetry (CV) consisting of 5 cycles, immediately followed by a linear sweep voltammetry (LSV), was conducted on all the samples.

The overpotential was calculated at 10 mA by subtracting the theoretical potential where the OER occurs (1.23 V). Pure CNTs were first tested as a blank sample (**Figure 3**a), and an overpotential was extracted (Figure 3c). However, these data were not taken into consideration further in this work as the main reaction happening is the carbon oxidation and not the oxidation of water. Concerning the coated samples, a reduction of the overpotential was recorded until reaching an optimized layer thickness (Figure 3b and **Table 2**) before increasing again. The overpotential of NiO appears to be independent of the film thicknesses up to 300 cycles. Beyond this point (400 cycles), a slight decrease is observed before increasing back. For the other samples, a minimum in overpotential is observed at number of ALD cycles corresponding to a film thickness of ≈2 nm. The optimized thicknesses for various catalyst compositions are summarized in Table 2.

The LSV analysis of the pure phases with an optimized thickness revealed the lowest activity toward the OER, displaying overpotentials of 443 and 323 mV at 10 mA for pure iron and nickel oxide, respectively (Figure 3a,b and c). In contrast, the LSV of the bimetallic catalysts, regardless of their composition, exhibited a higher activity (Figure 3a) and smaller overpotential (Figure 3c) compared to the pure phases. Figure 3c illustrates an overpotential decrease until reaching a minimal value (267 mV at 10 mA cm^{-2}) for 2Fe:1Ni, followed by a subsequent increase. The decrease followed by an increase in overpotential (estimated for a current density of 10 mA cm^{-2}) corresponds to the optimization of the iron and nickel atomic ratio. For some samples, the OER activity decreases more rapidly than others at higher current density (Figure 3a). The 2Fe:1Ni sample persisted as the most active catalyst even at current densities above 100 mA cm^{-2}.

The Tafel plots, at the same potential range, are shown in Figure S10, Supporting Information, and the Tafel slopes are summarized in Figure 3d. While a linear decrease until reaching an optimized atomic composition was expected, the Tafel slopes showed a different behavior. Indeed, the 1Fe:2Ni and 2Fe:1Ni both showed a fast electron transfer with a Tafel slope equal to 40.2 and 36.8 mV dec^{-1}, respectively. This suggests that the catalytic activity is influenced by other factors beyond the film composition and the surface concentration of the active sites. In addition, as shown in XPS and SAED analysis (Figure S2–S8, Supporting Information), the pure iron oxide film is composed of a crystalline phase (≈20% FeO) coexisting with an amorphous one (≈80% Fe_2O_3). It can be suggested that increasing the iron content in the deposited films leads to a higher percentage of amorphous phase. This leads to the conjecture that the nonlinear Tafel slope behavior can thus be explained by a competition between crystallinity and composition. Indeed, 1Fe:2Ni (most crystalline) and 2Fe:1Ni (optimized atomic ratio) exhibited, respectively, the fastest charge transfer.

Potentiostatic EIS was conducted for each sample, and the results are illustrated using a Nyquist plot (Figure 3e.1 and e.2, Figure S11, Supporting Information). In all the spectra, a linear segment is observed at high frequency due to the combination of the distributed ionic resistance and the distributed capacitance within the catalyst. Herein, the slight length of this segment indicates the reduced resistance of the catalyst layer. The linear segment is followed by one or two semi-circles representing the charge and mass transfer, respectively. For pure iron (Figure S8, Supporting Information), as well as for 3Fe:1Ni and 1Fe:2Ni, only one semi-circle is present, indicating that the frequencies at which the charge and the mass transfer occur overlap. Furthermore, the spectrum shape of 1Fe:1Ni, 3Fe:2Ni, and 2Fe:1Ni is similar, only their magnitude varies. The same remark can be done between the 1Fe:2Ni and the 3Fe:1Ni spectra. Those shape similarities imply that the catalysts respond in the same manner to the three electrochemical phenomena described previously. 2Fe:1Ni and 1Fe:2Ni exhibited the most interesting catalytic activity toward OER. The two samples displayed a comparable thickness (Table 2) suggesting that their performance is either due to the layer composition and/or to the crystallinity. Moreover, the SAED analysis (Figure S6, S7 and S8, Supporting Information) showed a consistent decrease of the crystallinity with the increase of the iron concentration. Notably, 1Fe:2Ni presents the highest crystallinity, while 3Fe:1Ni is the least crystalline. These results suggest that the high performance of the 1Fe:2Ni can be mostly attributed to its high crystallinity, whereas the one of the 2Fe:1Ni to its optimized composition.

As the 2Fe:1Ni sample displayed the most promising activity toward OER, chronoamperometry (CA) at 1.497 V was carried out (**Figure 4**d). The sample showed a high stability even after 15 h of constant applied potential. However, a decrease of current density around 20% was observed. This decrease cannot fully be associated with a decrease of the activity of the catalyst. Indeed, a partial detachment of the catalyst from the GCE was noted during the stability tests. High-resolution-TEM (HRTEM) images were acquired after the CA studies. They reveal a transformation in the catalyst morphology (Figure 4a,c and Figure S12, Supporting Information). Indeed, the remaining film on the CNTs became smoother. A comparison of the SAED diffraction patterns of the sample before and after CA (Figure 4a and b, Supporting Information) indicates a change in the crystalline

Table 2. Summary of the thickness of the optimized layer toward the OER for various thin film compositions.

Number of metallic pulses	Pulses ratio	Thickness of the optimized layer [nm]
400	0Fe:1Ni	5.60
200	1Fe:2Ni	1.75
300	1Fe:1Ni	1.77
400	3Fe:2Ni	1.8
400	2Fe:1Ni	1.64
300	3Fe:1Ni	1.77
200	1Fe:0Ni	1.64

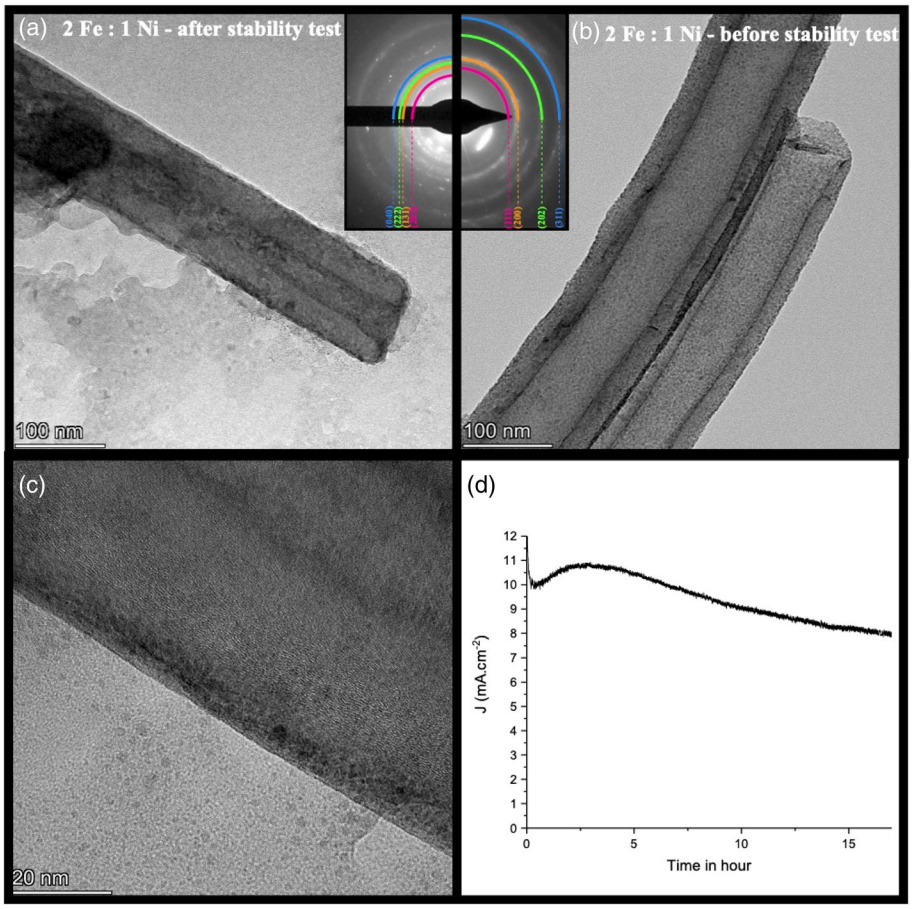

Figure 4. a) and b) TEM and SAED analysis of the 2Fe:1Ni sample after and before stability test; c) HRTEM of the same CNTs shown is (a); d) stability test of the 2Fe:1Ni sample.

phase. Indeed, after stability test, the Debye–Scherer rings can be attributed to the (202), (131), (222), and (040) reflections of a spinel-type $Ni_{1.4}Fe_{1.7}O_4$. This change of cristaline structure suggests an activation of the catalyst which leads to a more favorable electrochemical process.

3. Conclusion

Iron-nickel oxides and oxyhydroxides are known as highly effective catalysts for the OER in alkaline media. Although several synthesis routes have been reported to develop mixed iron nickel oxides, in this study for the first-time atomic layer deposition (ALD) was applied. A competition between the growth modes and the metal precursors was observed, leading to a minimal GPC for the 2Fe:1Ni super cycles. As the iron concentration increased, both the crystallinity and the roughness of the deposited layers decreased. The competition between the metal precursors and their growth modes was further supported by the observation of a nonlinear relationship between the metal pulses ratio and the iron and nickel relative concentration.

The optimized 2Fe:1Ni sample exhibited a significant catalytic activity toward the OER with an overpotential as low as 267 mV at 10 mA cm^{-2} and a Tafel slope of 36.8 mV dec^{-1}. Furthermore, it displayed a high stability even after 15 h of continuous operation.

To conclude, ALD is one of the techniques of choice to deposit iron nickel oxide oxygen evolution catalysts with good control of the thickness, composition, and crystallinity, allowing to propose clear composition–structure–properties correlations.

4. Experimental Section

Chemicals and Reagents: The CNTs were purchased from Pyrograf Products, Inc. The nitric acid (67%), the sulfuric acid (98%), and the hydrogen peroxide (30%) were acquired from VWR chemicals. Ferrocene ($Fe(Cp)_2$, 98%) has been purchased from Sigma-Aldrich. Nickelocene ($Ni(Cp)_2$, 98%) has been purchased from Strem. An ozone generator BMT803N and oxygen (99.98%, Air liquide) were employed to produce ozone. Argon (99.99%, Air liquide) was used as the carrier gas. Nafion5wt.% solution was acquired from Sigma-Aldrich. Alumina water-based slurries with particle sizes of 1 and 0.05 µm were acquired from Science services. The Alumina powder 0.03 µm was furnished by Metrohm with the glassy carbon electrode (GCE). The Nylon polishing cloth size 8" Dia. × N/H, PSA, and the Spec-Cloth, 8"xN/H, PS were purchased from Science Services.

Catalysts Fabrication: Before the ALD coating, the CNTs were functionalized according to the following process: 2 g of CNTs were submerged in 80 mL of nitric acid inside a tri-neck round bottom flask.[17,46]

The suspension was refluxed and heated at 105 °C in a silica oil bath during 6 h. After 6 h, the dispersion was let to cool down at room temperature. The CNTs were further collected and washed with distilled water until reaching a neutral pH by pump filtration. The CNTs were dried overnight at 60 °C in a vacuum oven. The CNTs were afterward dispersed in ethanol (10% ink) and sonicated (Super RK1028H, Sonorex) until obtaining a full dispersed and homogeneous suspension. The CNTs-ink was drop-casted on a microscope glass which was previously washed following the order: demineralized water (DI-water), 2-propanol, ethanol, and DI-water and then dried with a nitrogen gun. The drop-casted ink was left under fume hood until it dried.

Silicon wafers (Siegert Wafer B014002) were cut in 1 cm square and submerged in a piranha solution (¼ H_2O_2 and ¾ H_2SO_4) to remove any organic traces from their surface. After 20 min, the Si wafers were neutralized using demineralized water and were washed subsequently with DI-water, 2-propanol, ethanol, and DI-water, then dried with a nitrogen gun. Before ALD, the freshly cleaned silicon wafers were measured by ellipsometry.

The drop-casted CNTs and two clean silicon wafers were coated by ALD using a hot-wall GEMSTAR-6 Benchtop ALD system (ARRADIANCE, Inc.): Before starting the ALD-coating process, the samples were placed in the operating chamber under vacuum until reaching a stable value. The chamber, the organo-metallic precursors, and the manifolds were heated at 220, 90, and 120 °C, respectively. A constant flux of Ar equal to 10 sccm has been set up to retain a baseline pressure at 2.5×10^{-1} Torr. Before the beginning of the ALD processes, a second functionalization was carried out in situ: 10 pulses of ozone ($t_{pulse} = 300$ ms) without exposure time were applied to the samples. A waiting time in between each pulse was given to the chamber to fully recover the starting baseline pressure. Different supercycles (**Scheme 1**) were applied, where n and m are the number of ferrocene and nickelocene cycles, respectively. The different cycles used in the order n:m were equal to 0:1, 1:2, 1:1, 3:2, 2:1, 3:1, and 1:0. The organometallic precursors and ozone pulse times were 1000 ms and 300 ms, respectively. The ozone content during the pulses was set up at 20%wt. The exposure time used was equal to 30 s for each precursor, and the chamber was purged for 20 s. Concerning the number of supercycles applied (*x*), they were dependent of the number of organo-metallic pulses present in each semi cycle to always be composed of the same total number of metal precursors pulses, between 100 and 500 by steps of 100.

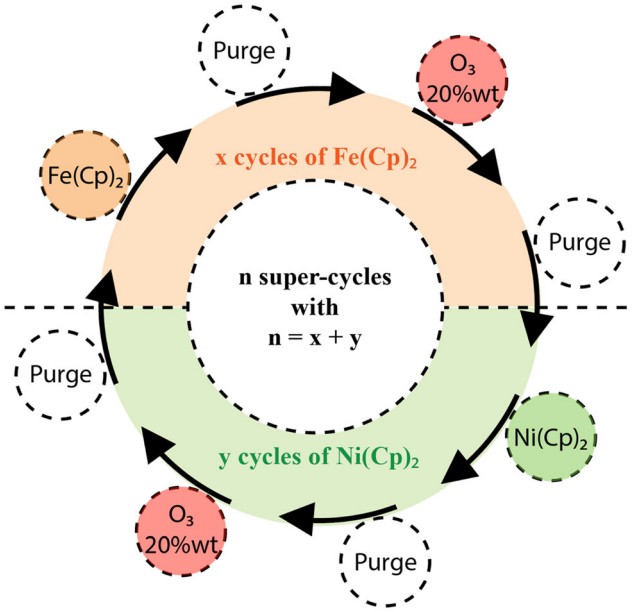

Scheme 1. Schematic explanation of an ALD supercycle.

Characterization: To determine the thickness conformity and the success of the deposition, the silicon wafers were analyzed before and after ALD by ellipsometry (SE). Then the data given were modeled using the SpectraRay-3 software (Cauchy-stack and Lorentz–Lorenz model for Fe_2O_3, NiO, and their supercycles).[3]

The CNTs were analyzed before ALD and after ALD by TEM, HRTEM, high-angle annular dark-field scanning transmission electron microscopy (HAADF-STEM), and energy-dispersive X-Ray analysis (EDX), with a FEI Talos F200S scanning/transmission electron microscope (S/TEM) operated at 200 kV. To produce the element maps, the FEI Velox software version 2.6. was used.

XPS data were measured at a JEOL JPS-9030 setup (base pressure 10^{-9} mbar), using an Mg X-Ray source ($h\nu = 1253.6$ eV) with 300 W excitation power. A pass energy of 50 eV was used for the survey scans, and a pass energy of 30 eV was used for the narrow scans, yielding an overall setup resolution of 1.3 eV, as determined from the width of the Ag $3d_{5/2}$ peak (310 meV natural line width assumed). The binding energy scale of the setup was calibrated by setting the Au $4f_{7/2}$ of a gold foil to 84.0 eV and the Cu $2p_{3/2}$ of a copper foil to 932.66 eV. Since some samples showed a static charging, we have set the binding energy of the C 1s C—C peak of the CNTs to 285.0 eV for a better comparison between the samples. All the powder samples were evenly and thinly distributed on carbon tape in air. The sensitivity factors (SSF) were calculated from the atomic cross sections, the elemental inelastic mean free path, and the measured transmission function, SSF_Ni2$p_{-3/2}$ = 17.55 and SSF_Fe2$p_{-3/2}$ = 12.06. An iterative Shirley background was chosen for all spectra.[47]

Electrochemical Measurements: The electrochemical measurements were carried out on a Bio-Logic VMP3 potentiostat/galvanostat equipped with a built-in electrochemical impedance spectroscopy (EIS) analyzer. All the electrochemical tests were performed with the help of a three-electrode electrochemical cell. A GCE (from Metrohm) with a 3 mm diameter tip adapted to the rotating disc electrode from Metrohm was used as a working electrode (WE). A platinum wire was used as a counter electrode and an Ag/AgCl electrode from Metrohm as a reference.

Before any electrochemical measurement, the GCE was polished and cleaned according to the following process. Two drops of alumina slurry 1 µm were deposited on the nylon polishing cloth and diluted with some additional MilliQ water drops. The GCE was then maintained perpendicularly to the substrate and gently polished in 8 motions 30 times approximately. The same process was repeated using the 0.05 and the 0.03 µm alumina slurry. Afterward, to remove any residual alumina slurry from the glassy carbon surface, the electrode was gently clean on the spec cloth pre-wet with absolute ethanol. The GCE tip was then gently washed with absolute ethanol followed by MilliQ water before being dried under a nitrogen flow.

In parallel, the catalyst ink has been prepared by mixing 3 mg of catalyst with 450 µL MilliQ water/ethanol (1:1) and 50 µL of Nafionsolution. The obtained ink was sonicated until the obtention of a homogeneous dispersion of the CNTs. 2×2 µL (total 4 µL) were taken from the freshly prepared ink and were drop-casted on the glassy carbon disc (=0.071 cm^2) of the GCE (equal to a 0.25 mg cm^{-2} loading). The OER measurements were performed at room temperature in a 1 M KOH solution with a rotation of the WE of 1600 rpm. CV experiments were carried out between 0 and 0.6 V (potential window) with a scan rate equal to 20 mV s^{-1}. The CV was repeated 5 times per samples and directly followed by LSV. The LSV was performed between 0 and 0.7 V with a scan rate of 5 mV s^{-1}. Subsequently to the LSV, an EIS under potentiostatic control (PEIS) of 5 mV was carried out between 100 kHz and 100 mHz at 0.547 V vs RHE.

The LSV data were subsequently converted to reversible hydrogen electrode potential using the equation (3), then corrected for the ohmic drop using the equation (4)

$$E_{RHE} = E_{Ag/AgCl} + E^{\circ}_{Ag/AgCl} + 0.059\,V * pH \quad (3)$$

$E_{Ag/AgCl}$ = applied potential, $E^{\circ}_{Ag/AgCl}$ = standard potential of the Ag/AgCl electrode in 1 M KOH = 0.2 V, pH of the electrolyte = 13.6

$$iR\,\text{drop} = (J * 0.07 * \Omega)/1000 \quad (4)$$

J = measured current density in mA cm^{-2}, 0.07 cm^2 = surface of the GCE, Ω = resistance during the PEIS at $t = 0$.

A chronoamperometry at 10 mA cm^{-2} was carried out on the catalyst that exhibited the most promising activity toward OER to study its stability. The same setup as described previously was used. After the stability test, the layer was collected using a disposable micro spatula and dispersed in ethanol to be analyzed by TEM, HRTEM, and SAED.

Supporting Information

Supporting Information is available from the Wiley Online Library or from the author.

Acknowledgements

Dr. Patricia Russo is acknowledged for her support and advices, Christoph Erdmann for the TEM studies, and Fionn Collins for his help and support.

Conflict of Interest

The authors declare no conflict of interest.

Data Availability Statement

The data that support the findings of this study are available from the corresponding author upon reasonable request.

Keywords

atomic layer deposition, growth modes, nickel and iron oxides, oxygen evolution reaction in alkaline media

Received: March 20, 2024
Revised: July 12, 2024
Published online: September 3, 2024

[1] J. P. Van Hook, *Catal. Rev., Sci. Eng.* **1980**, *21*, 1.
[2] T. Shinagawa, A. T. Garcia-Esparza, K. Takanabe, *Sci. Rep.* **2015**, *5*, 12801.
[3] C. Spöri, J. Tai Hong Kwan, A. Bonakdarpour, D. P. Wilkinson, P. Strasser, *Angew. Chem., Int. Ed.* **2017**, *56*, 5994.
[4] C. Wei, Z. J. Xu, *Small Methods* **2018**, *2*, 1800168.
[5] H. G. Sanchez Casalongue, M. Ling Ng, S. Kaya, D. Friebel, H. Ogasawara, A. Nilson, *Angew. Chem., Int. Ed.* **2014**, *53*, 7169.
[6] N. Mamaca, E. Mayousse, S. Arrii-Clacens, T. W. Napporn, K. Servat, N. Guillet, K. B. Kokoh, *Appl. Catal., B* **2012**, *111–112*, 376.
[7] M. H. Miles, E. A. Klaus, B. P. Gunn, J. R. Locker, W. E. Serafin, S. Srinivasan, *Electrochem. Acta* **1978**, *23*, 521.
[8] S. Anantharaj, S. R. Ede, K. Sakthikumar, K. Karthick, S. Mishra, S. Kundu, *ACS Catal.* **2016**, *6*, 8069.
[9] R. Blomme, R. Ramesh, L. Henderick, M. Minjauw, P. Vereecken, M. Adriaens, C. Detavernier, J. Dendooven, *Nanotechnology* **2024**, *35*, 235401.
[10] Y. Li, H. He, W. Fu, C. Mu, X.-Z. Tang, Z. Liu, D. Chi, X. Hu, *Chem. Commun.* **2016**, *52*, 1439.
[11] B. K. Kang, M. H. Woo, J. Lee, Y. H. Song, Z. Wang, Y. Guo, Y. Yamauchi, J. H. Kim, B. Lim, D. H. Yoon, *J. Mater. Chem. A* **2017**, *5*, 4320.
[12] M. A. Oliver-Tolentino, J. Vázquez-Samperio, A. Manzo-Robledo, R. de Guadalupe González-Huerta, J. L. Flores-Moreno, D. Ramírez-Rosales, A. Guzmán-Vargas, *J. Phys. Chem. C* **2014**, *118*, 22432.
[13] C. Tang, H.-S. Wang, H.-F. Wang, Q. Zhang, G.-L. Tian, J.-Q. Nie, F. Wie, *Adv. Mater.* **2015**, *27*, 4516.
[14] M. H. Raza, K. Movlaee, Y. Wu, S. M. El-Refaei, M. Karg, S. G. Leonardi, G. Neri, N. Pinna, *ChemElectroChem* **2019**, *6*, 383.
[15] K. L. Nardi, N. Yang, C. F. Dickens, A. L. Strickler, Stacey F. Bent, *Adv. Energy Mater.* **2015**, *5*, 1500412.
[16] A. Dutta, S. Mutyala, A. K. Samantara, S. Bera, B. K. Jena, N. Pradhan, *ACS Energy Lett.* **2018**, *3*, 141.
[17] C. Huai, C. Xi, A. Hu, Y. Zhang, Z. Xu, D. Nordlund, C.-J. Sun, C. A. Cadigan, R. M. Richards, L. Li, C.-K. Dong, X.-W. Du, F. Lin, *J. Am. Chem. Soc.* **2021**, *143*, 18519.
[18] L. Trotochaudn, S. L. Young, J. K. Ranney, S. W. Boettcher, *J. Am. Chem. Soc.* **2014**, *136*, 6744.
[19] Z. Cai, D. Zhou, M. Wanf, S.-M. Bak, Y. Wu, Z. Wu, Y. Tian, X. Xiong, Y. Li, W. Liu, S. Siahrostami, Y. Kuang, X.-Q. Yanf, H. Duan, Z. Feng, H. Wang, X. Sun, *Angew. Chem.* **2018**, *130*, 9536.
[20] C. Peng, N. Ran, G. Wan, W. Zhao, Z. Kuang, Z. Lu, C. Sun, J. Liu, L. Wang, H. Chen, *ChemSusChem* **2020**, *13*, 811.
[21] F. Song, M. M. Busch, B. Lassalle-Kaiser, C.-S. Hsu, E. Petkucheva, M. Bensimon, H. M. Chen, C. Corminboeud, X. Hu, *ACS Cent. Sci.* **2019**, *5*, 558.
[22] A. P. Espejo, R. Zierold, J. Gooth, J. Dendooven, C. Detavernier, J. Escrig, K. Nielsch, *Nanotechnology* **2016**, *27*, 345707.
[23] Y. T. Chong, E. M. Y. Yau, K. Nielsch, J. Bachmann, *Chem. Mater.* **2010**, *22*, 6506.
[24] N. Pinna, M. Knez, in *Atomic Layer Deposition of Nanostructured Materials*, Wiley-VCH, Weinheim, Germany **2011**
[25] M. Ritala, M. Leskelä, in *Handbook of Thin Films*, Academic Press, San Diego, CA **2002**.
[26] S. M. George, *Chem. Rev.* **2010**, *110*, 111.
[27] S. Chen, J. Duan, P. Bian, Y. Tang, R. Zheng, S.-Z. Qiao, *Adv. Energy Mater.* **2015**, *5*, 1500936.
[28] R. L. Puurunen, *Chem. Vap. Deposition* **2003**, *9*, 249.
[29] R. W. Johnson, A. Hultqvist, S. F. Bent, *Mater. Today* **2014**, *17*, 236.
[30] R. L. Puurunen, W. Vandervorst, *Jpn. J. Appl. Phys* **2004**, *96*, 7686.
[31] C. Marichy, M. Bechelany, N. Pinna, *Adv. Matter.* **2012**, *24*, 1017.
[32] C. Mariachy, N. Pinna, *Coord. Chem. Rev.* **2013**, *257*, 3232.
[33] S. A. Kukushkin, A. V. Osipov, A. I. Romanychev, *Phys. Solid State* **2016**, *58*, 1448.
[34] K. B. Klepper, O. Nilsen, H. Fjellvågn, *J. Cryst. Growth* **2007**, *307*, 457-
[35] Y. Fan, Y. Wu, G. Clavel, M. H. Raza, P. Amsalem, N. Koch, N. Pinna, *ACS. Appl. Energy Mater.* **2018**, *1*, 4554.
[36] X. Tong, Y. Qin, X. Guo, O. Moutanabbir, X. Ao, E. Pippel, L. Zhang, M. Knez, *Small* **2012**, *8*, 3390.
[37] A. B. F. Martinson, M. J. DeVries, J. A. Libera, S. C. Christensen, J. T. Hupp, M. J. Pellin, J. W. Elam, *J Phys. Chem. C* **2011**, *115*, 4333.
[38] J. Liu, B. Xiao, M. N. Banis, R. Li, T.-K. Sham, X. Sun, *Electrochim. Acta* **2015**, *162*, 275.
[39] C. Marichy, J.-P. Tessonnier, M. C. Ferro, K.-H. Lee, R. Schlögl, N. Pinna, M.-G. Willinger, *J. Mater. Chem.* **2012**, *22*, 7323.
[40] L. M. Dyagileva, V. P. Mar'in, E. I. Tsyganova, G. A. Razuvaev, *J. Organomet. Chem.* **1979**, *175*, 63.
[41] J. M. O'Connor, C. P. Casey, *Chem. Rev.* **1987**, *87*, 307-
[42] J. Okudan, in *Transition Metal Coordination Chemistry. Topics in Current Chemistry* (Ed: W. A. Herrmann), Springer, Berlin, Heidelberg **2005**.

[43] M. Rooth, A. Johanson, K. Kukli, J. Aarik, M. Boman, A. Mårsa, *Chem. Vap. Deposition* **2008**, *14*, 67.
[44] M. C. Biesinger, L. W. M. Lau, A. R. Gerson, R. S. C. Smart, *Phys. Chem. Chem. Phys.* **2012**, *14*, 2434.
[45] M. C. Biesinger, B. P. Payne, A. P. Grosvenor, L. W. M. Lau, A. R. Gerson, R. S. C. Smart, *Appl. Surf. Sci. 257*, **2011**, 2717.
[46] S. J. Roosendaal, PhD Thesis, Utrecht University, **1999**
[47] M. P. Seah, W. A. Dench, *Surf. Interface Anal.* **1979**, *1*, 2.